Research Article Vol. 32, No. 16 / 29 Jul 2024 / *Optics Express* 28035

Optics EXPRESS

Broadband rapid-scanning phase-modulated Fourier transform electronic spectroscopy

ARIBA JAVED,[1,†] **JULIAN LÜTTIG,**[1,†] **STEPHANIE E. SANDERS,**[1,†] **FRANCESCO SESSA,**[1,†] **ALASTAIR T. GARDINER,**[2] **MANUEL JOFFRE,**[3] **AND JENNIFER P. OGILVIE**[1,4,*]

[1] *Department of Physics, University of Michigan, 450 Church St., Ann Arbor, MI 48109, USA*
[2] *Laboratory of Anoxygenic Phototrophs, Institute of Microbiology of the Czech Academy of Sciences, Třeboň, Czech Republic*
[3] *Laboratoire d'Optique et Biosciences, Ecole Polytechnique, CNRS, INSERM, Institut Polytechnique de Paris, 91128 Palaiseau, France*
[4] *Department of Physics, University of Ottawa, 150 Louis-Pasteur Pvt, Ottawa, ON, K1N 6N5, Canada*
[†] Equal author contributions
[*] *jogilvie@umich.edu*

Abstract: We present a phase-modulated approach for ultrabroadband Fourier transform electronic spectroscopy. To overcome the bandwidth limitations and spatial chirp introduced by acousto-optic modulators (AOMs), pulses from a 1 µm laser are modulated using AOMs prior to continuum generation. This phase modulation is transferred to the continuum generated in a yttrium aluminum garnet crystal. Separately generated phase-modulated continua in two arms of a Mach-Zehnder interferometer interfere with the difference of their modulation frequencies, enabling physical under-sampling of the signal and the suppression of low-frequency noise. By interferometrically tracking the relative time delay of the continua, we perform continuous, rapid-scanning Fourier transform electronic spectroscopy with a high signal-to-noise ratio and spectral resolution. As proof of principle, we measure the linear absorption and fluorescence excitation spectra of a laser dye and various biological samples.

1. Introduction

In its most common implementation, Fourier transform (FT) spectroscopy employs two replicas of an optical field with a variable time delay to measure a spectral response in the time-domain. Upon Fourier transformation of the time-domain interferogram, the spectrum is retrieved in the frequency domain. Compared to dispersive spectrometers, FT spectrometers avoid grating losses and can offer higher signal-to-noise ratios under some conditions, a fact that is known as "Fellgett's advantage" [1]. They can also offer higher spectral resolution [2]. Additionally, all wavelengths are simultaneously measured on a single element detector, which can offer faster read-out speeds than multi-element arrays. Recently, wide-field hyperspectral imaging has been achieved via FT spectroscopy from every pixel of a camera [3]. FT spectroscopy optimizes the time-frequency resolution trade-off [4], and forms the basis for the powerful multidimensional FT spectroscopies that originated in the NMR community and are now widely used in the infrared and visible regimes. FT spectroscopy requires interferometric precision with path length stabilities of ~λ/100 to obtain reliable frequency axes and separate complex signal components with high signal-to-noise ratios [5]. Conventional Mach-Zehnder (MZ) or Michelson interferometers work well in the infrared, where the wavelengths are long, but are often unstable in the visible regime. Common solutions to ensure interferometric stability in the visible regime for electronic spectroscopy include birefringent interferometers [6,7], passive [8,9] or active stabilization [10–16], spectrometers based on gratings [17], pulse shapers [18–22] as well as interferometric tracking of the delay [23–26]. Phase-modulation is an alternative

#530991 https://doi.org/10.1364/OE.530991
Journal © 2024 Received 23 May 2024; revised 20 Jun 2024; accepted 23 Jun 2024; published 18 Jul 2024

approach that improves the stability by decoupling the time delay of an optical pulse pair from its relative phase [27]. Phase-modulation Fourier transform spectroscopy (PM-FTS) has been used in a variety of techniques, including fluorescence-detected wavepacket interferometry [28], as well as a growing number of multidimensional spectroscopies, including coherent [29] and "action-detected" modalities. Action-detected PM-FTS methods have employed fluorescence [30–32], photocurrent [33,34] and photo-ion [35] detection. The extreme sensitivity of PM-FTS-based multidimensional spectroscopy has been demonstrated through measurements of dilute gases [35] and solutions [36] as well as ultracold atoms [37,38]. Phase-modulation has also enabled spatially-resolved multidimensional spectroscopic measurements [30,39].

In phase-modulation, an acousto-optic modulator (AOM) imparts a distinct radio frequency (RF) shift, modulating the pulse-to-pulse carrier-envelope phase. Linear or non-linear spectroscopic signals of interest can be isolated using lock-in detection [27,31], super-heterodyne mixing [40], and digital lock-in approaches [41–43], as well as methods optimized for rapid imaging applications [44]. However, AOMs decrease in efficiency with increasing bandwidth of the input light. In addition, the different wavelengths will diffract at slightly different angles, imparting spatial chirp [45]. Spatial chirp can be reduced through careful optimization of focusing conditions [36], and can be overcome by double-passing the AOM at the expense of throughput [29,46]. These considerations limit the spectroscopic bandwidth that can be achieved with AOM-based techniques [47]. Expanding the bandwidth of PM-FTS would broaden its applications in multiple techniques, such as linear and multidimensional spectroscopy and hyperspectral imaging [3,47]. Here we present an approach that circumvents the bandwidth limitations of AOMs by applying the modulation to the pump laser prior to continuum generation, producing broadband pulses that are modulated at the AOM frequency. A similar concept has been used to extend PM-fluorescence-detected two dimensional spectroscopy into the ultraviolet (UV) in which phase-modulation prior to second harmonic generation produced the required phase-modulated UV pulse sequence [48]. As a proof of principle, we perform linear absorption and fluorescence excitation measurements of a laser dye (IR140) and biological samples, including myoglobin, bacteriochlorophyll *a* (BChl *a*) and whole purple bacterial cells.

1.1. Phase-modulated continuum generation

To understand the effect of phase modulation on continuum generation, we consider a periodic train of laser pulses with a repetition rate of f_{rep} and a corresponding time $T_{\mathrm{rep}} = 1/f_{\mathrm{rep}}$ between laser pulses. Sending the pulse train through an AOM that is modulated at a frequency Ω_i imparts a phase modulation, shifting the carrier-envelope phase by an increment of $\Omega_i T_{\mathrm{rep}}$ between consecutive pulses. We can describe the electric field of the m^{th} pulse in the pulse train as [27,31]:

$$E_m(t) = A_m(t - mT_{\mathrm{rep}}) \cos[\omega_0(t - mT_{\mathrm{rep}}) + m\Omega_i T_{\mathrm{rep}}] \tag{1}$$

where $A_m(t - mT_{\mathrm{rep}})$ is the pulse envelope and ω_0 is the laser center frequency. To understand how AOM phase modulation of the relatively narrowband pump laser impacts continuum generation, consider the Kerr effect in the yttrium aluminum garnet (YAG) crystal. As the electric field of the laser pulse traverses the crystal, it produces an intensity dependent refractive index n:

$$n(t) = n_0 + n_2 |E_m(t)|^2 \tag{2}$$

where n_0 is the linear refractive index, n_2 is the nonlinear refractive index of the material, and $|E_m(t)|^2$ is the intensity of the incident electric field [49]. The relevant phenomenon that leads to super-continuum generation in condensed media is self-phase modulation [49,50], which describes the phase change caused by the time-dependent index of refraction $\Delta n(t) = n(t) - n_0$ in propagating through the medium. Assuming uniform focusing through the material of length l, self-phase modulation introduces a phase change of

$$\Delta\varphi(t) = \frac{\omega_0 n_2}{c}|E_m(t)|^2 l \tag{3}$$

resulting in a corresponding frequency broadening $\Delta\omega(t) = -\partial(\Delta\varphi)/\partial t$. The output spectrum of the generated continuum is given by

$$|E_m(\omega)|^2 = \left|\int_0^\infty E_m(t)e^{-i\omega_0 t + i\Delta\varphi(t)}dt\right|^2 \tag{4}$$

Within the slowing-varying approximation, i.e., $(\omega_0\tau_p \gg 1)$, where τ_p is the pulse duration, the rapidly oscillating terms in the integral will not contribute, and the broadening of the spectrum is determined by the time-dependence of the pulse envelope. The initial phase of the electric field given in Eq. (1) is still carried by the pulse during and after traveling through the medium, resulting in a broadened phase-modulated continuum. We note that our argument above is highly simplistic, assuming uniform focusing throughout the medium and ignoring other phenomena such as self-focusing, multi-photon ionization, and avalanche ionization [51] that can modify the broadening effect. However, assuming any third-order optical nonlinear process, even non-instantaneous, the relevant generated field will be proportional to $\mathcal{E}_m(t)\mathcal{E}_m^*(t')\mathcal{E}_m(t'')$, where $\mathcal{E}_m(t)$ is the complex electric field. The continuum will thus carry a phase $m\Omega_i T_{\text{rep}} - m\Omega_i T_{\text{rep}} + m\Omega_i T_{\text{rep}} = m\Omega_i T_{\text{rep}}$, as predicted by the simplified model above. Furthermore, it has been previously demonstrated that independent white-light continua generated from the same laser source exhibit spectral interference, confirming the preservation of their relative phase after continuum generation [52].

The first implementations of linear and two-dimensional PM-FTS employed a step-scan, lock-in detection approach, recording the signals of interest by locking onto reference signals oscillating at the signal frequency [27,31]. These reference signals were constructed from the spectrally-narrowed unused interferometer output which oscillates at the difference in AOM frequencies of the two interferometer arms. Use of the spectrally-narrowed reference signal enables physical under-sampling of the signal, making PM-FTS insensitive to mechanical noise. We previously demonstrated a continuous scan, digital lock-in approach to phase-modulated fluorescence detected two-dimensional electronic spectroscopy (F-2DES) [42]. In the digital lock-in method we simultaneously digitize multiple signals via a Data Acquisition (DAQ) Board. These signals include the signal from the sample, the spectrally-narrowed phase reference signal, and a mixer signal that measures the RF frequency difference of the AOMs in each interferometer. The mixer signal allows one to track any drifts in AOM frequency and to isolate signal contributions at the linear combination of the RF frequencies. The signals are recorded in the time domain at the laser repetition rate as the time delay between the two pulses is continuously varied. However, to retrieve the correct frequency axes, the precise time delay between the two arms must be known to interferometric precision. This can be obtained directly from the spectrally-narrowed phase reference signal which is recorded in parallel with the sample signal, interferometrically tracking the precise phase difference between the two arms of the interferometer during the continuous scan [42].

2. Experimental methods

The basis for broadband PM-FTS is a MZ interferometer with two unique features: phase modulation with AOMs and continuum generation in each arm, as shown in Fig. 1(a). The output from a 1040 nm, 1 MHz Ytterbium amplified laser (Spectra Physics Spirit-HE, 280 fs pulse duration) is split using a 50/50 beam splitter (Evaporated Coating Inc. 1040-1600 nm, 3 mm thick), sending 3.75 W into each arm of the MZ interferometer. The reflected beam passes through a N-BK7 window (3 mm thick) to compensate for the difference in dispersion compared to the reflected arm. The 1040 nm fundamental is diffracted by an AOM (Isomet

M1346-aQ(fc) -H) in each arm. We chose AOMs containing quartz crystal for its high optical damage threshold of ∼12 GW/cm^2 to withstand the orders of magnitude higher input power compared to previous implementations of PM-FTS in which continuum generation preceded the AOM modulation step [30,42]. The first diffracted order, which is modulated with the driving RF frequency of the AOM, is used for continuum generation. We adjust the amplitude of each RF signal, such that the first diffracted order in each arm has the same average power (∼1 W). The non-diffracted zeroth order beams (∼3W) are safely dumped into beam blocks (Thorlabs LB2) using D-shaped mirrors. Unique modulation frequencies are generated by two outputs from an RF signal generator (Novatech, 409B, 1 kHz resolution), and amplified to ∼50 W (Mini-Circuits, ZHL-100W-52-s+) before being sent to the AOMs. The amplifiers operate in the linear regime to avoid influence from higher harmonics. For our measurements, we used Ω_0 = 80 MHz and Ω_1 = 79.977 MHz, resulting in signal that modulates at the difference of the AOM frequencies (23 kHz). To account for drifts in the AOM driving frequencies, we take a portion of each output from the RF generator and send them to a radio frequency mixer (Mini-Circuits, ZAD-1-1+) to track fluctuations during the measurements.

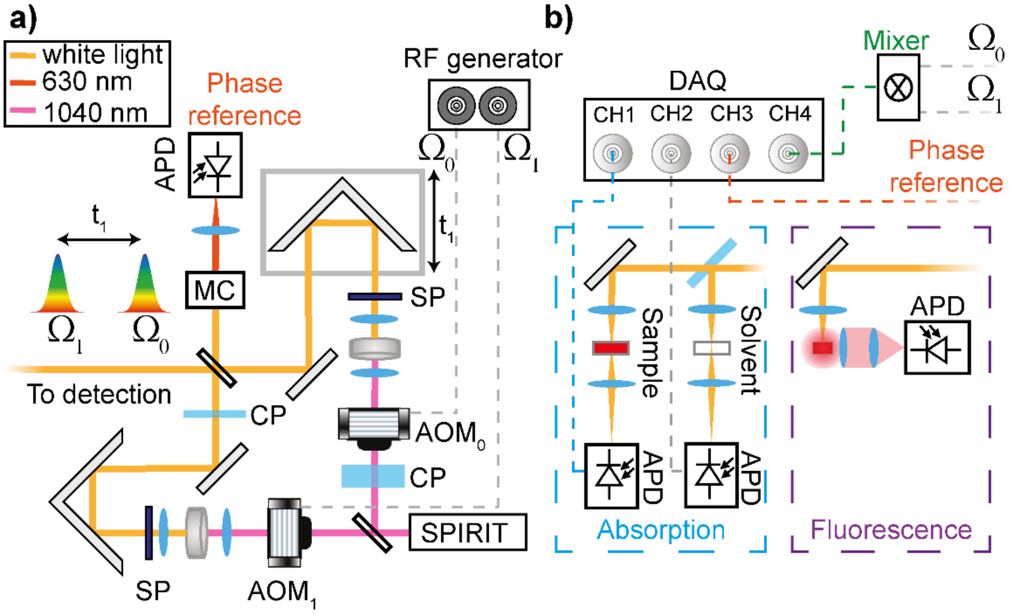

Fig. 1. Experimental setup of the ultrabroadband continuous-scanning phase-modulated spectrometer: a) the Mach-Zehnder (MZ) interferometer with an acousto-optic modulator (AOM) modulated at Ω_i, and continuum generation in each arm. Short pass filters (SP) remove residual fundamental. One output of the MZ goes to detection, whereas the other is spectrally narrowed with a monochromator (MC) and measured on an avalanche photodiode (APD) for phase reference. b) An overview of the signals collected on the data acquisition card (DAQ). Two possible detection geometries are shown. For absorption (blue outline), the signal of the sample and the solvent are collected simultaneously. For fluorescence (purple outline), only the signal in the 90° detection geometry is collected.

The phase-modulated first order diffracted beams are focused into YAG crystals (8 mm thick, Newlight Photonics) using 5 cm focal length lenses (Thorlabs LA1131-AB) to generate supercontinua in each arm of the MZ [53]. The beam size, power, and focusing conditions are adjusted to be comparable between the two arms to produce continua that are as spectrally similar as possible. The beams are then collimated with 2.5 cm focal length lenses (Thorlabs

LA1951-AB) and the residual fundamental light is filtered out using 950 nm short pass filters (Thorlabs, FESH0950). The final spectra of our continua in the visible span ~500-950 nm, with the red edge determined by the short pass filters. Each arm is directed into a retroreflector. Arm 1 is fixed, whereas the retroreflector in Arm 0 is mounted on a mechanical delay stage (Newport, M-VP25XL) to vary the relative time delay. The two arms are then recombined with a 50/50 beam splitter, chosen to have a smooth and flat spectral response (Layertec, 106896, 1 mm thick). A NBK7 window (1 mm thick) is placed in Arm 1 before recombination to compensate for the additional dispersion added to Arm 0 from the recombining beam splitter. One output of the MZ interferometer is spectrally narrowed to 2.4 nm FWHM centered at 630 nm using a monochromator (Optometric, DMC1-03). The intensity of the spectrally narrowed two-pulse interference signal is measured on a photodiode (Thorlabs PDA36A), serving as the phase reference for interferometric tracking of the time delay. In principle, any spectrally narrowed wavelength can be used for the phase reference. However, we found that using a bluer wavelength was helpful for resolving the signal in the blue edge of the spectrum. This is illustrated in Fig. S6 where we report a comparison of the retrieved laser spectrum versus reference wavelength. The other output of the MZ interferometer is directed to the sample for absorption or fluorescence measurements as described below.

2.1. Data collection

The two sample signal collection geometries for absorption and fluorescence excitation measurements are shown in Fig. 1(b). The sample of interest is placed in the “sample arm”. For absorption measurements an additional reference spectrum is required to remove the effect of the laser spectrum and solvent absorption. This is achieved by picking off a small fraction of the beam in the sample arm using a 3 mm thick uncoated window and directing it into the “solvent arm” to simultaneously measure the sample and reference spectra. This additional reference was omitted for the fluorescence measurements, but could also be implemented to remove the laser spectrum from the fluorescence excitation spectrum if desired. As depicted in Fig. 1(b), four signals are collected for linear absorption measurements via a DAQ card (National Instruments, NI-USB 6366): the sample signal, the solvent reference, the phase reference, and the mixer signal. For the fluorescence measurements only three channels were collected, omitting the solvent reference. The experiments were performed with continuous, rapid scanning of the time delay by moving the mechanical stage back and forth at a speed of 0.1 mm/s and with an acceleration of 100 mm/s^2 about time zero, which was determined using spectral interferometry. The total scanning range was -800 to 800 fs, yielding a spectral resolution of 1.25 THz (~2 nm).

For the linear absorption measurements, both the sample and solvent signals are focused onto photodiodes (Thorlabs PDA36A2) with 5 cm focal length achromatic lenses (Thorlabs AC254-050-AB). We perform two consecutive measurements to extract the linear absorption spectrum from our PM-FTS set-up. First, we measure solvent in both the “sample arm” and the “solvent arm” to account for any spectral differences in the two arms or any differences in the detectors. Then, we perform a second measurement where the solvent in the “sample arm” is replaced with the sample of interest. If any drift of the continuum occurs, we correct for it using both detection arms. Using the two measurements, we calculate the absorbance of the sample using:

$$\mathrm{OD} = \underbrace{\log_{10}\left[\frac{I_{\mathrm{solv}}^{\mathrm{solv.\ arm}}}{I_{\mathrm{sam}}^{\mathrm{sam.\ arm}}}\right]}_{\text{Measurement 2}} - \underbrace{\log_{10}\left[\frac{I_{\mathrm{solv}}^{\mathrm{solv.arm}}}{I_{\mathrm{solv}}^{\mathrm{sam.\ arm}}}\right]}_{\text{Measurement 1}} \tag{5}$$

where I denotes the intensity of the Fourier transformed signal in the frequency domain of the corresponding arm and sample as described below. The superscripts “sam. arm” and “solv. arm” represent the sample and the solvent arms respectively and the subscripts “sam” and “solv” stand for the measured cuvette contents in each arm. The four intensity I terms were obtained following the linear signal processing algorithm described in further detail in Supplement 1.

For the fluorescence excitation measurements, the emitted fluorescence signal is collected in the 90° detection geometry by a 2 inch diameter, 100 mm focal length lens, and then focused onto an avalanche photodiode (Hamamatsu, c12703-01). Any scattered laser light is blocked with long pass filters in front of the detector. Additionally, short pass filters are placed before the sample to remove wavelengths not absorbed by the sample to further minimize contributions from scattered laser light. The solvent arm without any sample or solvent was used as a reference arm using a photodiode (Thorlabs PDA36A2) to monitor the continuum throughout the experiment. The reported absorption and laser spectra have been corrected for the detector response. Because the detected fluorescence bandwidth is small, the detector correction was not applied in the case of the fluorescence excitation measurements. Additionally, laser spectra as well as fluorescence spectra reported in wavelength were scaled according to the appropriate Jacobian transformation [54]. This factor is omitted in the case of the absorption spectra since they are reported in optical density, i.e., as the ratio between two spectra. The Jacobian transformation ensures that the integral of the laser spectra and fluorescence spectra which is proportional to the energy is kept constant while transforming from wavelength to frequency. A detailed description of the data processing using the signals from the sample arm, solvent arm, phase reference, and mixer is given in Supplement 1.

3. Results/discussion

3.1. Experiment characterization

In Fig. 2(a) we show a typical time domain interferogram representing the intensity cross-correlation measurement of the two continua. The interferogram was measured with a total acquisition time of 2 min, for a total of 48 back-and-forth scans of the time delay (Fig. 2(a) inset, red curves). The back-and-forth scans are well overlapped, validating the accuracy of the interferometric time delay tracking. Before Fourier transformation, we average all the scans in the time domain (Fig. 2(a), black curve). The asymmetry of the interferogram stems from differences in the spectral phase of the two continua. While we aimed to match the dispersion of the two arms of the MZ, it is likely that the focus positions in the 8 mm YAG crystals are slightly different, yielding similar spectra with different spectral phases. The retrieved cross-correlation spectrum obtained from the Fourier transform of the time-domain signal is shown in Fig.2b (blue dashed curve). For comparison we show in Fig. 2(b) a representative spectrum of the continuum from one arm of the MZ measured via a commercial fiber-coupled spectrometer (Ocean Optics, USB-2000). The spectrum is typical for continuum generation via YAG spanning from ~ 500–950 nm with a maximum intensity of ~600 nm. The continuum also reaches into the near-infrared [53], but is truncated in our setup by the short pass filter at 950 nm used to remove the fundamental. Our measured cross-correlation spectrum with PM-FTS agrees well with the reference spectrum for long wavelengths, while the intensity of the shorter wavelengths is reduced in the PM-FTS spectrum. The discrepancy at short wavelengths is due to intensity and relative phase fluctuations of the white light continua which are generally less stable at wavelengths farthest from the fundamental. To characterize the spectral differences and the stability of the two continua, we collected 500 spectra with 3 ms integration time on the Ocean Optics spectrometer for both arms with the AOM frequencies matched to observe spectral interference (Fig. S3), and separate spectra for each arm (Fig. S4). There is clear spectral interference across nearly the entire bandwidth in any single spectrum measured in Fig. S3, with poorer fringe contrast at shorter wavelengths. Fig. S4 shows that the spectra of the two arms are very similar, and exhibit significant intensity fluctuations at shorter wavelengths.

We first demonstrate the technical capabilities of our setup, such as measurement time and sensitivity, on a dye, IR140 (Exciton), in ethanol. The absorption spectrum of IR140 consists

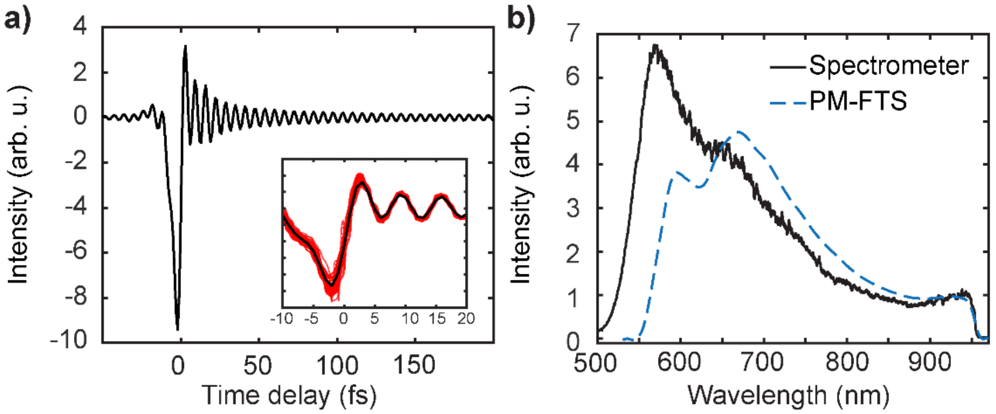

Fig. 2. a) Time-domain interferograms retrieved from the two-pulse interference output of the MZ, using a reference wavelength of 630 nm. Data corresponding to 48 back and forth stage scans is shown (inset, solid red line). Average of the 48 scans used for calculating the cross-correlation power spectrum is also shown (black line). b) The cross-correlation power spectrum retrieved using the broadband PM-FTS setup (dashed blue line), plotted against the spectrum measured using a commercial spectrometer (Ocean Optics, USB-2000) after recombination from the MZ (black line).

of one single broad absorption peak with its maximum at ~820 nm (Fig. 3(a) and (b), black solid line). For the absorption measurements of IR140, we used a 1 mm pathlength cuvette. In Fig. 3(a), we compare our retrieved absorption spectrum via PM-FTS for several measurement times using a sample with OD of 0.03 and a combined pulse energy of 10 pJ. All the traces were extracted from a single dataset of 48 total back and forth scans. The 2 min of measurement time trace corresponds to averaging all 48 scans, while fractions of the full dataset (12 scans and 1 scan) were averaged corresponding to 30 sec and 2.5 sec of data collection. In all cases, the spectral shape and intensity of the spectrum measured with PM-FTS is consistent with the spectrum measured with a commercial dispersive UV-Vis spectrometer. The signal-to-noise ratio (SNR) is visibly lower for the 2.5 sec measurement as expected, but we can still resolve the main absorption peak well. Increasing the data acquisition time to 30 sec, we see a dramatic improvement in SNR. The experimental measurement time for high SNR data could be further reduced by increasing the stage speed. In Fig. 3(b), we characterize the sensitivity of our setup for measuring low concentrations by diluting the IR140 sample to a maximum OD of 0.016 and 0.008 (light blue lines) and comparing the normalized absorption spectra to the normalized spectrum of IR140 with an OD of 0.03 measured with PM-FTS (dark blue line) and a commercial UV-Vis spectrometer (black line). The main absorption feature is reproduced well for both dilutions. While our setup can still resolve the main absorption feature for the lowest concentration, it has reduced accuracy in the regions with very low absorbance. However, for the concentration corresponding to an OD of 0.016, a comparable SNR to approximately double the concentration is observed. Furthermore, we performed measurements at different pulse energies as shown in Supplement 1 demonstrating that we can retrieve spectra with reasonable SNR with combined pulse energies of 1 pJ to 15 pJ. The ability to perform rapid measurements with low excitation energies is particularly important for samples that are susceptible to photodamage [55] or for avoiding higher-order effects such as exciton-exciton annihilation [56].

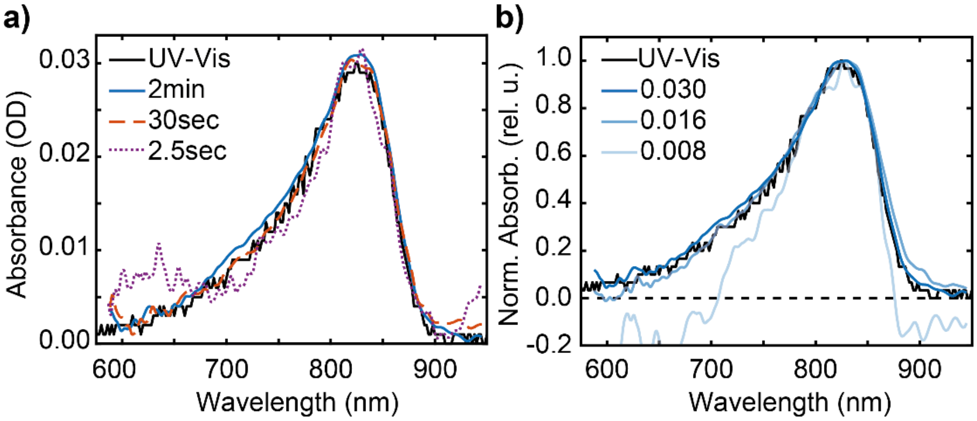

Fig. 3. Comparison of linear absorption measurements of IR140 made by PM-FTS and a commercial UV-Vis spectrometer: a) Acquisition time dependence for IR140 with an OD of 0.03. The blue solid, red dashed and purple dotted curve were extracted by only averaging over part of the full dataset corresponding to 2 min, 30 sec, and 2.5 sec of measurement time respectively. b) Concentration dependence (measurement time of 2 minutes).

3.2. Linear absorption of biological pigments

The PM-FTS setup is broadly applicable to a myriad of samples absorbing in the range of ~ 550 nm to 950 nm. We further illustrate its capabilities by making linear absorption measurements on several biological samples. As a first example, we study different oxidation species of myoglobin. Myoglobin was the first protein to have its X-ray structure determined [57]. It is primarily located in the muscles where it acts as an oxygen storage protein. The oxidized form of myoglobin, metmyoglobin has a characteristic brown color, while binding molecular oxygen results in the red oxymyoglobin species. We prepared metmyoglobin and oxymyoglobin in potassium phosphate buffer as described in Supplement 1. In Fig. 4(a), we show the absorption spectra measured via PM-FTS (dashed lines) as well as via a commercial UV-Vis spectrometer (solid lines), showing good agreement between the two methods. While both samples have little to no absorption from 700 nm to 950 nm, we can clearly distinguish oxy- from metmyoglobin from the spectral features on the blue edge of the spectrum. As seen by the laser spectrum (grey) in Fig. 4(a), the retrieved cross-correlation spectrum had little spectral intensity in the blue region during these measurements, limiting the spectral range to >600 nm. A combination of poor relative phase and intensity stability of the continua in the blue results in diminished spectral interference in this wavelength range, which is further discussed in Supplement 1. We note that an extensive study of the relative phase stability of dual continua generated in YAG reports larger deviations at shorter wavelengths, consistent with our observations [58]. Extending the measurement further into the blue could be achieved by improving the continuum stability and generating the continuum in other materials, such as CaF_2 which are capable of generating bluer continua [59]. We note that our current cross-correlation continuum spectrum shows some variation between days, as seen by the different laser spectra shown in Fig. 4(a) and (b), which changes the measurable spectral range.

As an additional sample we studied BChl *a*, one of the main pigments in the photosynthetic apparatus of bacteria such as heliobacteria, green sulfur bacteria and purple bacteria [60]. The structure of BChl *a* consists of a central bacteriochlorin unit coordinating a Mg^{2+}-ion. The bacteriochlorin unit gives rise to two distinct absorption bands: a strong absorption at ~800 nm called Q_y and a weaker absorption at ~600 nm called Q_x [61]. Additionally, the absorption spectrum exhibits a strong vibronic shoulder of the Q_y peak at ~700 nm. The measured absorption

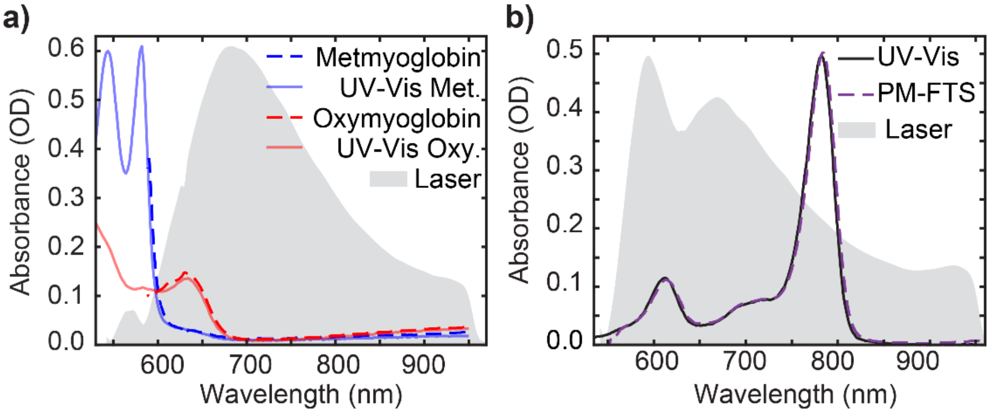

Fig. 4. Linear absorption spectra of biological pigments measured via PM-FTS. a) Metmyoglobin (dashed blue line) and oxomyoglobin (dashed red line) compared to the linear absorption measurement of the two species recorded by a commercial UV-Vis spectrometer (solid blue and red lines). The PM-FTS measurement time was 2 minutes. b) BChl *a* (dashed purple line) compared to the absorption spectrum of BChl *a* measured using a UV-Vis spectrometer (solid black line). We also show the laser spectra acquired via PM-FTS that was used to perform both experiments (shaded gray area).

via UV-Vis spectrometer (solid black line) and via PM-FTS (dashed purple line) in Fig. 4(b) show excellent agreement, highlighting the accuracy of the PM-FTS approach.

3.3. Linear fluorescence excitation of biological pigments

In addition to linear absorption measurements, we also acquired linear fluorescence excitation spectra using PM-FTS. The information content is comparable to linear absorption measurements, but fluorescence detection can have some advantages for fluorescent molecules and scattering samples. Fluorescence measurements are background-free, enabled by spectral filtering and the ability to collect signal in the 90° geometry. To avoid any scattering from the excitation beams reaching the detector, we used additional short pass filters before the sample. The fluorescence excitation spectrum of BChl *a* (Fig. 5(a), purple dashed line) shows the same characteristic features as the linear absorption spectrum. The peak ratio is different between the linear fluorescence excitation and absorption measurements reflecting the fact that the fluorescence excitation spectrum is modulated by the spectral shape of the cross-correlation spectrum (Fig. 5(a)). We note that because we do not remove the laser spectrum, our reported fluorescence excitation spectra are the product of the fluorescence excitation spectrum $g(\omega)$ and the cross-correlation spectrum of the continua. In principle, this could be removed by simultaneously collecting a cross-correlation reference spectrum similar to the “solvent arm” in the absorption measurements.

Due to the background-free nature of fluorescence detection, measuring fluorescence excitation spectra with PM-FTS has great promise for highly scattering samples, such as whole cells. As a proof of principle, we measured the fluorescence excitation spectrum of whole cells of the purple bacterium *Rhodoblastus acidophilus*. While the primary absorber in purple bacteria is BChl *a*, the absorption spectrum of the whole cells exhibits additional peaks and spectral shifts compared to the absorption spectrum of monomeric BChl *a* [Fig. 5(a)]. These arise from the antenna and reaction center pigment-protein complexes in which the protein environment tunes the BChl *a* transitions and controls excitonic coupling between the pigments. The spectrum exhibits two main absorption bands above 750 nm: one at 800 nm which corresponds to the absorption of the B800 band of light-harvesting complex 2 (LH2), and a broader absorption peaking at 850-875 nm

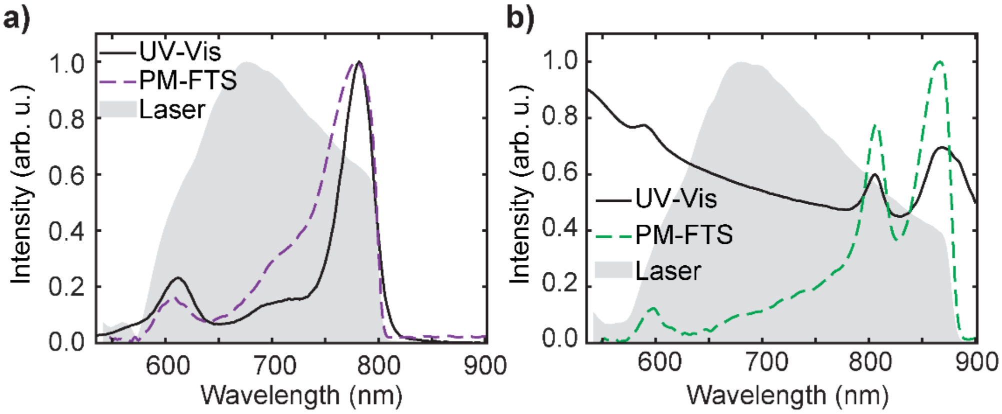

Fig. 5. Fluorescence excitation spectra of biological samples measured via PM-FTS. a) Linear fluorescence excitation spectra of BChl *a* (dashed purple line) along with linear absorption spectra recorded by a commercial UV-Vis spectrometer (solid black line). We also show the cross-correlation laser spectrum acquired via PM-FTS that was used to perform the experiment (shaded gray). The spectrum was cut at 800 nm for BChl *a* with an appropriate short pass filter to minimize scattering. b) Linear fluorescence excitation of *purple* bacteria (dashed green line) compared to the linear absorption measurement recorded by a commercial UV-Vis (solid black line). Note that the UV-Vis spectrum has a large background due to scatter, which is eliminated in the fluorescence measurement. We also show the cross-correlation laser spectrum that was used to perform the experiment (shaded gray). The spectrum was cut at 875 nm via a short pass filter.

containing the B850 band of LH2 and the absorption of light-harvesting complex 1 (LH1) as well as the absorption of the reaction center (RC). Furthermore, we can identify the absorption of Q_x at ~600 nm arising from the BChl *a* present in LH1, LH2 and the RC. Although these features are identifiable in the absorption spectrum using a UV-Vis spectrometer (Fig. 5(b), black solid line), they are less pronounced due to the large background from scattering. In the fluorescence excitation spectrum (dashed green line), the significant scattering contribution is avoided by using short pass filter before the sample (in this case at 875 nm, Fig. 5(b), gray curve) as well as long pass filters for the fluorescence. This result highlights the advantages of fluorescence detection for studying highly scattering samples and the promise of PM-FTS for hyperspectral imaging of whole cells.

4. Conclusion

Here we have demonstrated broadband PM-FTS, surpassing the bandwidth of previous implementations by applying the AOM phase modulation prior to continuum generation. We demonstrate that the AOM phase modulation of the fundamental carries over to the continuum generation, enabling us to perform PM-FTS measurements with a high SNR in the wavelength range from ~550–950 nm. The rapid and continuous-scanning nature of the experiment coupled with simultaneous signal, mixer, and phase reference collection allows us to interferometrically track the delay time. The additional simultaneous collection of the cross-correlation laser spectrum allows for compensation of any changes in the supercontinuum to minimize the effects of spectral drift. We demonstrated the capabilities of our setup on a variety of samples including laser dyes and biological pigments. We illustrated the sensitivity of our setup by resolving an absorption spectrum within 2.5 sec, with low OD, and with low excitation energies. In addition to linear absorption measurements, we demonstrated PM-FTS measurements of fluorescence excitation spectra which is especially powerful for highly scattering samples, such as whole purple bacterial cells. The ability of our method to measure spectra with fast acquisition times and low excitation intensity is well-suited for reducing photobleaching during measurements. Our setup could be easily combined with other broadband sources, such as CaF_2-generated continua, extending the available spectrum further to shorter wavelengths. We note that a recent multidimensional experiment demonstrated active phase-stabilization of a white-light continuum using phase modulation via AOMs [62]. In contrast to our approach, the AOMs act not on the white-light beam directly but on a reference beam, enabling active stabilization of the relative phase of the time-delayed pulse pair for step-scanned measurements. In our continuous scan approach the phase modulation is transferred to the signal itself, enabling physical under-sampling of the signal.

In addition to the linear absorption and fluorescence excitation spectroscopy presented here, broadband rapid-scanning PM-FTS could be incorporated into other techniques such as multidimensional spectroscopy and hyperspectral imaging. The broad bandwidth of our method is especially important in multidimensional spectroscopy where it enables studies of diverse processes such as coherent dynamics and energy transfer between spectrally separated states [63–65]. For example, our PM-FTS setup could be extended to broadband phase-modulated fluorescence-detected two-dimensional spectroscopy. We note that pulse compression, which is unimportant here for linear measurements, would be necessary for multidimensional spectroscopies. We have previously shown that dispersion mismatch between the interferometer arms, which is significant in the data presented here, can be readily measured and corrected in phase-modulated fluorescence-detected two-dimensional spectroscopy [42]. While broadband multidimensional spectroscopy has been achieved [66–69], so far a broadband phase modulation approach is lacking. Such an approach would allow us to correlate spectrally separated peaks such as Q_x and Q_y transitions of chlorophyll based excitonic systems, as we have done previously in coherent and fluorescence-detected two-dimensional electronic spectroscopy with a 1 kHz repetition rate [70,71]. Phase-modulation approaches are particularly powerful for enabling fully collinear multidimensional spectroscopy, enabling hyperspectral imaging or spatially-resolved multidimensional spectroscopy [29,30,72].

Funding. Air Force Office of Scientific Research (FA9550-18-1-0343); Office of Science (DE-SC0016384); Directorate for Mathematical and Physical Sciences (PHY-1914608); Human Frontier Science Program (LT0056/2024-C).

Disclosures. The authors declare no conflicts of interest.

Data availability. Data underlying the results presented in this paper are not publicly available at this time but may be obtained from the authors upon reasonable request.

Supplemental document. See Supplement 1 for supporting content.

References

1. L. Mertz, *Transformations in Optics* (John Wiley & Sons, 1965).
2. P. R. Griffiths and J. A. de Haseth, *Fourier Transform Infrared Spectrometry* (John Wiley & Sons, 2007).
3. A. Perri, B. E. N. de Faria, D. C. T. Ferreira, *et al.*, "Hyperspectral imaging with a TWINS birefringent interferometer," Opt. Express **27**(11), 15956–15967 (2019).
4. P. Hamm and M. Zanni, *Concepts and Methods of 2D Infrared Spectroscopy* (Cambridge University Press, 2011).
5. D. M. Jonas, "Two-Dimensional Femtosecond Spectroscopy," Annu. Rev. Phys. Chem. **54**(1), 425–463 (2003).
6. D. Brida, C. Manzoni, and G. Cerullo, "Phase-locked pulses for two-dimensional spectroscopy by a birefringent delay line," Opt. Lett. **37**(15), 3027–3029 (2012).
7. J. Réhault, M. Maiuri, A. Oriana, *et al.*, "Two-dimensional electronic spectroscopy with birefringent wedges," Rev. Sci. Instrum. **85**(12), 123107 (2014).
8. M. L. Cowan, J. P. Ogilvie, and R. J. D. Miller, "Two-dimensional spectroscopy using diffractive optics based phased-locked photon echoes," Chem. Phys. Lett. **386**(1-3), 184–189 (2004).
9. T. Brixner, T. Mančal, I. V. Stiopkin, *et al.*, "Phase-stabilized two-dimensional electronic spectroscopy," J. Chem. Phys. **121**(9), 4221–4236 (2004).
10. M. U. Wehner, M. H. Ulm, and M. Wegener, "Scanning interferometer stabilized by use of Pancharatnam's phase," Opt. Lett. **22**(19), 1455–1457 (1997).
11. D. Grassani, M. Galli, and D. Bajoni, "Active stabilization of a Michelson interferometer at an arbitrary phase with subnanometer resolution," Opt. Lett. **39**(8), 2530–2533 (2014).

12. B. Huber, S. Pres, E. Wittmann, *et al.*, "Space- and time-resolved UV-to-NIR surface spectroscopy and 2D nanoscopy at 1 MHz repetition rate," Rev. Sci. Instrum. **90**(11), 113103 (2019).
13. T. Zhang, C. N. Borca, X. Li, *et al.*, "Optical two-dimensional Fourier transform spectroscopy with active interferometric stabilization," Opt. Express **13**(19), 7432–7441 (2005).
14. W. P. de Boeij, M. S. Pshenichnikov, and D. A. Wiersma, "Heterodyne-detected stimulated photon echo: applications to optical dynamics in solution," Chem. Phys. **233**(2-3), 287–309 (1998).
15. V. Volkov, R. Schanz, and P. Hamm, "Active phase stabilization in Fourier-transform two-dimensional infrared spectroscopy," Opt. Lett. **30**(15), 2010–2012 (2005).
16. N. F. Scherer, A. J. Ruggiero, M. Du, *et al.*, "Time resolved dynamics of isolated molecular systems studied with phase-locked femtosecond pulse pairs," J. Chem. Phys. **93**(1), 856–857 (1990).
17. P. V. Kolesnichenko, L. Wittenbecher, and D. Zigmantas, "Fully symmetric dispersionless stable transmission-grating Michelson interferometer," Opt. Express **28**(25), 37752–37757 (2020).
18. C. Li, W. Wagner, M. Ciocca, *et al.*, "Multiphoton femtosecond phase-coherent two-dimensional electronic spectroscopy," J. Chem. Phys. **126**(16), 164307 (2007).
19. P. Tian, D. Keusters, Y. Suzaki, *et al.*, "Femtosecond phase-coherent two-dimensional spectroscopy," Science **300**(5625), 1553–1555 (2003).
20. J. A. Myers, K. L. M. Lewis, P. F. Tekavec, *et al.*, "Two-color two-dimensional Fourier transform electronic spectroscopy with a pulse-shaper," Opt. Express **16**(22), 17420–17428 (2008).
21. D. B. Turner, K. W. Stone, K. Gundogdu, *et al.*, "Invited Article: The coherent optical laser beam recombination technique (COLBERT) spectrometer: coherent multidimensional spectroscopy made easier," Rev. Sci. Instrum. **82**(8), 081301 (2011).
22. E. M. Grumstrup, S.-H. Shim, M. A. Montgomery, *et al.*, "Facile collection of two-dimensional electronic spectra using femtosecond pulse-shaping technology," Opt. Express **15**(25), 16681–16689 (2007).
23. C. J. Buchenauer and A. R. Jacobson, "Quadrature interferometer for plasma density measurements," Rev. Sci. Instrum. **48**(7), 769–774 (1977).
24. L. P. DeFlores, R. A. Nicodemus, and A. Tokmakoff, "Two-dimensional Fourier transform spectroscopy in the pump-probe geometry," Opt. Lett. **32**(20), 2966–2968 (2007).
25. N. Belabas and M. Joffre, "Visible-infrared two-dimensional Fourier-transform spectroscopy," Opt. Lett. **27**(22), 2043–2045 (2002).
26. L. Lepetit and M. Joffre, "Two-dimensional nonlinear optics using Fourier-transform spectral interferometry," Opt. Lett. **21**(8), 564–566 (1996).
27. P. F. Tekavec, T. R. Dyke, and A. H. Marcus, "Wave packet interferometry and quantum state reconstruction by acousto-optic phase modulation," J. Chem. Phys. **125**(19), 194303 (2006).
28. N. F. Scherer, R. J. Carlson, A. Matro, *et al.*, "Fluorescence-detected wave packet interferometry: Time resolved molecular spectroscopy with sequences of femtosecond phase-locked pulses," J. Chem. Phys. **95**(3), 1487–1511 (1991).
29. T. L. Purz, E. W. Martin, W. G. Holtzmann, *et al.*, "Imaging dynamic exciton interactions and coupling in transition metal dichalcogenides," J. Chem. Phys. **156**(21), 214704 (2022).
30. V. Tiwari, Y. A. Matutes, A. T. Gardiner, *et al.*, "Spatially-resolved fluorescence-detected two-dimensional electronic spectroscopy probes varying excitonic structure in photosynthetic bacteria," Nat. Commun. **9**(1), 4219 (2018).
31. P. F. Tekavec, G. A. Lott, and A. H. Marcus, "Fluorescence-detected two-dimensional electronic coherence spectroscopy by acousto-optic phase modulation," J. Chem. Phys. **127**(21), 1 (2007).
32. C. L. Smallwood, R. Ulbricht, M. W. Day, *et al.*, "Hidden silicon-vacancy centers in diamond," Phys. Rev. Lett. **126**(21), 213601 (2021).
33. K. J. Karki, J. R. Widom, J. Seibt, *et al.*, "Coherent two-dimensional photocurrent spectroscopy in a PbS quantum dot photocell," Nat. Commun. **5**(1), 5869 (2014).
34. G. Nardin, T. M. Autry, K. L. Silverman, *et al.*, "Multidimensional coherent photocurrent spectroscopy of a semiconductor nanostructure," Opt. Express **21**(23), 28617–28627 (2013).
35. L. Bruder, U. Bangert, M. Binz, *et al.*, "Coherent multidimensional spectroscopy of dilute gas-phase nanosystems," Nat. Commun. **9**(1), 4823 (2018).
36. A. Sahu, V. N. Bhat, S. Patra, *et al.*, "High-sensitivity fluorescence-detected multidimensional electronic spectroscopy through continuous pump-probe delay scan," J. Chem. Phys. **158**(2), 024201 (2023).
37. D. F. Liang, L. S. Rodriguez, H. T. Zhou, *et al.*, "Optical two-dimensional coherent spectroscopy of cold atoms," Opt. Lett. **47**(24), 6452–6455 (2022).
38. F. Landmesser, T. Sixt, K. Dulitz, *et al.*, "Two-dimensional electronic spectroscopy of an ultracold gas," Opt. Lett. **48**(2), 473–476 (2023).
39. T. Jakubczyk, V. Delmonte, M. Koperski, *et al.*, "Radiatively limited dephasing and exciton dynamics in $MoSe_2$ monolayers revealed with four-wave mixing microscopy," Nano Lett. **16**(9), 5333–5339 (2016).
40. T. M. Autry, G. Moody, J. Fraser, *et al.*, "Single-scan acquisition of multiple multidimensional spectra," Optica **6**(6), 735–744 (2019).
41. K. Karki, M. Torbjornsson, J. R. Widom, *et al.*, "Digital cavities and their potential applications," J. Instrum. **8**(05), T05005 (2013).

42. D. Agathangelou, A. Javed, F. Sessa, *et al.*, "Phase-modulated rapid-scanning fluorescence-detected two-dimensional electronic spectroscopy," J. Chem. Phys. **155**(9), 094201 (2021).
43. D. Uhl, L. Bruder, and F. Stienkemeier, "A flexible and scalable, fully software-based lock-in amplifier for nonlinear spectroscopy," Rev. Sci. Instrum. **92**(8), 083101 (2021).
44. T. L. Purz, S. T. Cundiff, and E. W. Martin, "Lock-in detector for accelerated nonlinear imaging," Opt. Lett. **46**(19), 4813–4816 (2021).
45. D. J. McCarron, "A Guide to Acousto-Optic Modulators," http://themccarrongroup.com/wp-content/uploads/2020/03/AOM-Guide.pdf.
46. E. A. Donley, T. P. Heavner, F. Levi, *et al.*, "Double-pass acousto-optic modulator system," Rev. Sci. Instrum. **76**(6), 063112 (2005).
47. F. D. Fuller and J. P. Ogilvie, "Experimental Implementations of Two-Dimensional Fourier Transform Electronic Spectroscopy," Annu. Rev. Phys. Chem. **66**(1), 667–690 (2015).
48. J. R. Widom, N. P. Johnson, P. H. von Hippel, *et al.*, "Solution conformation of 2-aminopurine dinucleotide determined by ultraviolet two-dimensional fluorescence spectroscopy," New J. Phys. **15**(2), 025028 (2013).
49. Y. R. Shen and G.-Z. Yang, "Theory of Self-Phase Modulation and Spectral Broadening," in *The Supercontinuum Laser Source*, R. R. Alfano, ed. (Springer New York, 1989), pp. 1–32.
50. R. R. Alfano, *The Supercontinuum Laser Source: Fundamentals with Updated References* (Springer New York, 2006).
51. L. Bergé, S. Skupin, R. Nuter, *et al.*, "Ultrashort filaments of light in weakly ionized, optically transparent media," Rep. Prog. Phys. **71**(10), 109801 (2008).
52. M. Bellini and T. W. Hänsch, "Phase-locked white-light continuum pulses: toward a universal optical frequency-comb synthesizer," Opt. Lett. **25**(14), 1049–1051 (2000).
53. N. M. Kearns, R. D. Mehlenbacher, A. C. Jones, *et al.*, "Broadband 2D electronic spectrometer using white light and pulse shaping: noise and signal evaluation at 1 and 100 kHz," Opt. Express **25**(7), 7869–7883 (2017).
54. J. Mooney and P. Kambhampati, "Get the basics right: Jacobian conversion of wavelength and energy scales for quantitative analysis of emission spectra," J. Phys. Chem. Lett. **4**(19), 3316–3318 (2013).
55. A. Vogel, J. Noack, G. Hüttman, *et al.*, "Mechanisms of femtosecond laser nanosurgery of cells and tissues," Appl. Phys. B **81**(8), 1015–1047 (2005).
56. J. Pšenčík, Y.-Z. Ma, J. B. Arellano, *et al.*, "Excitation energy transfer dynamics and excited-state structure in chlorosomes of Chlorobium phaeobacteroides," Biophys. J. **84**(2), 1161–1179 (2003).
57. J. C. Kendrew, R. E. Dickerson, B. E. Strandberg, *et al.*, "Structure of myoglobin: a three-dimensional Fourier synthesis at 2 Å resolution," Nature **185**(4711), 422–427 (1960).
58. B. Maingot, G. Chériaux, N. Forget, *et al.*, "Spectral coherence properties of continuum generation in bulk crystals," Opt. Express **30**(12), 20311–20320 (2022).
59. C. Nagura, A. Suda, H. Kawano, *et al.*, "Generation and characterization of ultrafast white-light continuum in condensed media," Appl. Opt. **41**(18), 3735–3742 (2002).
60. R. E. Blankenship, *Molecular Mechanisms of Photosynthesis* (Wiley, 2002).
61. Y. Song, A. Schubert, E. Maret, *et al.*, "Vibronic structure of photosynthetic pigments probed by polarized two-dimensional electronic spectroscopy and ab initio calculations," Chem. Sci. **10**(35), 8143–8153 (2019).
62. M. S. Barclay, N. D. Wright, P. Cavanaugh, *et al.*, "Ultrabroadband two-dimensional electronic spectroscopy in the pump–probe geometry using conventional optics," Opt. Lett. **49**(8), 2065–2068 (2024).
63. J. Dostál, J. Pšenčík, and D. Zigmantas, "In situ mapping of the energy flow through the entire photosynthetic apparatus," Nat. Chem. **8**(7), 705–710 (2016).
64. P. F. Tekavec, J. A. Myers, K. L. M. Lewis, *et al.*, "Two-dimensional electronic spectroscopy with a continuum probe," Opt. Lett. **34**(9), 1390–1392 (2009).
65. A. Niedringhaus, V. R. Policht, R. Sechrist, *et al.*, "Primary processes in the bacterial reaction center probed by two-dimensional electronic spectroscopy," Proc. Natl. Acad. Sci. **115**(14), 3563–3568 (2018).
66. X. Ma, J. Dostál, and T. Brixner, "Broadband 7-fs diffractive-optic-based 2D electronic spectroscopy using hollow-core fiber compression," Opt. Express **24**(18), 20781–20791 (2016).
67. E. Harel, P. D. Long, and G. S. Engel, "Single-shot ultrabroadband two-dimensional electronic spectroscopy of the light-harvesting complex LH2," Opt. Lett. **36**(9), 1665–1667 (2011).
68. D. Timmer, D. C. Lünemann, S. Riese, *et al.*, "Full visible range two-dimensional electronic spectroscopy with high time resolution," Opt. Express **32**(1), 835–847 (2024).
69. G. Bressan, I. A. Heisler, G. M. Greetham, *et al.*, "Half-broadband two-dimensional electronic spectroscopy with active noise reduction," Opt. Express **31**(25), 42687–42700 (2023).
70. S. E. Sanders, M. Zhang, A. Javed, *et al.*, "Expanding the bandwidth of fluorescence-detected two-dimensional electronic spectroscopy using a broadband continuum probe pulse pair," Opt. Express **32**(6), 8887–8902 (2024).
71. H. H. Nguyen, E. Maret, Y. Song, *et al.*, "Charge separation in the photosystem II reaction center revealed by multipsectral multidimensional spectroscopy," Sci. Adv. **9**, eade7190 (2022).
72. S. Goetz, D. Li, V. Kolb, *et al.*, "Coherent two-dimensional fluorescence micro-spectroscopy," Opt. Express **26**(4), 3915–3925 (2018).